Improved Device Performance of Interband Cascade Lasers with Hybrid Cladding Layers Operating in the 3 to 4 µm Wavelength Region

Yixuan Shen,[1] Jeremy A. Massengale,[1,2] Rui Q. Yang,[1,+] Tetsuya D. Mishima,[2] and Michael B. Santos[2]

[1] School of Electrical and Computer Engineering, University of Oklahoma, Norman, OK
[2]Homer L. Dodge Department of Physics and Astronomy, University of Oklahoma, Norman, OK USA 73019.

[+] Author for correspondence: Rui.q.Yang@ou.edu

Abstract

In this work, we briefly review the development and status of interband cascade lasers (ICLs) as related to long-standing issues due to the InAs/AlSb superlattice cladding. By focusing on a hybrid cladding approach to alleviate these issues, we demonstrate substantially improved device performance of ICLs compared to earlier reported ICLs of a similar design in the 3 to 4 µm wavelength region. These improvements include a threshold current density for broad-area devices as low as 134 A/cm^2 at 300 K and reduced threshold voltage with a peak voltage efficiency of 80%, which is more than 10% higher than that obtained from previously reported ICLs. Moreover, we have demonstrated continuous wave (cw) operation of a broad-area device up to 278 K, the highest cw operating temperature among epi-side up mounted broad-area type-II ICLs, implying improved thermal dissipation with the hybrid cladding approach. Additionally, by conducting a comparative study of ICLs with different GaSb layer thicknesses in the hole injector, we reveal and discuss an interesting correlation between the carrier transport, threshold voltage, and hole-induced absorption loss, which may help to guide device optimization for operation in a targeted temperature range.

Keywords: interband cascade; quantum well; semiconductor lasers; mid-infrared; waveguide.

1. Introduction and Brief Review

Interband cascade lasers (ICLs) [1-2] are constructed by taking advantage of the broken-gap alignment in III-V Sb-based heterostructures [3-4] to form a cascade configuration that reuses every injected electron to emit multiple photons with a high quantum efficiency as shown in Fig. 1. The ICL's cascade feature is similar to the one used by a quantum cascade laser (QCL), which is based on intersubband transitions [5] within the conduction band. In contrast to the QCL, the ICL is based on electronic transitions across the bandgap between the conduction (C) and valence (V) bands (Fig. 1) so that the fast phonon scattering inherent in QCLs is circumvented. As such, the population inversion can be more easily established between two interband transition states with a much longer carrier lifetime (~ns) compared to a short lifetime (~ps or shorter) in QCLs. Consequently, together with the cascade injection, ICLs have a significantly reduced threshold current density and voltage, translating to a low power consumption. Also, the emission wavelength of ICLs with type-II quantum well (QW) active regions can be tailored to cover an entire mid-infrared (IR) spectrum (*e.g.*, 3 to 15 μm) by merely adjusting QW layer thicknesses.

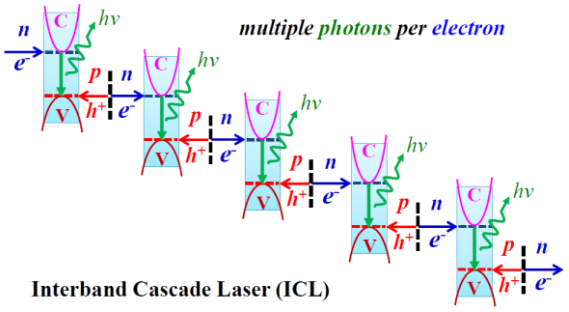

Fig. 1 Schematic illustration of an ICL, in which dashed lines indicate semi-metallic interfaces where electrons and holes are generated internally duo to the broken-bandgap alignment in type-II heterostructure.

Since the first proposal of the ICL concept at a conference in 1994 [1,2], followed by encouraging modeling results [6] and insightful assessments from equivalent circuit perspectives [7] in 1996, as well as the first experimental demonstration in early 1997 [8], enormous progress has been made in the development of ICLs [9-24]. This has occurred despite the relative immaturity of the Sb-based material system and an incomplete understanding of the best practices for epitaxial growth and device fabrication/packaging techniques. Type-II ICLs now exhibit excellent device performance in continuous wave (cw) operation at temperatures up to 115°C with low threshold-current densities (*e.g.*, 100 A/cm^2 at 300 K) [18, 20], low power consumption (<0.1 W at threshold at 300 K), high output power (exceeding 500 mW at 300K [19]), with wavelength coverage from 2.7 to 6.2 μm at room temperature (RT) in cw operation [21-24]. In general, ICLs are an attractive mid-IR source for many applications such as free-space optical communication, industrial process control, chemical sensing, environmental and greenhouse gas monitoring, and food safety. The RT threshold-input-power density of recent ICLs is as low as 0.35 kW/cm^2, an order of magnitude lower than that reported for the best QCL [15, 20], indicating the superiority of ICLs as energy-efficient mid-IR light sources for practical applications. For example, single-mode distributed feedback (DFB) ICLs [25-27] have been developed and used in the laboratory, on aircraft and high-altitude balloon instruments, and on the Mars Curiosity rover for measuring H_2CO, C_2H_6, C_2H_4, CO, atmospheric CH_4 and HCl profiles [28-35]. To date, efficient operation of type-II ICLs grown on both GaSb and InAs substrates have been demonstrated above RT in the wavelength range from 4 to 6 μm [21-24, 36-38]. However, extending this efficiency to wavelengths spanning the 6 μm to 15 μm region is more challenging and is being addressed by InAs-based ICLs using a plasmon waveguide approach [21, 39-41] and an innovative design for the QW active region [42-44], which has resulted in initial demonstration of lasing up to 14.4 μm [44].

Although excellent device performance has been achieved in the wavelength range from 3 to 6 μm, there are several outstanding issues in GaSb-based type-II ICLs that arise from the use of thick (several microns) InAs/AlSb short-period superlattice (SL) cladding layers. The SL cladding region typically has more than 2000 interfaces and is very demanding for growth by molecular beam epitaxy (MBE) with so many shutter movements. Also, it may be difficult to achieve high-quality strain-balanced material because of possible beam flux variations over very long (many hours) growth runs. Furthermore, this InAs/AlSb

SL has a low thermal conductivity κ (~3 W/m·K [45-47]) and thick SL layers cause considerable accumulation of heat, which limits the output power of ICLs and may also lead to reliability issues with local strain and thermal stress. Additionally, the SL cladding layer has a refractive index (~3.37) that is only slightly smaller than that of the cascade region (3.43 to 3.47), so the cladding layer must be quite thick to properly confine the optical wave. Reducing this thickness would lead to substantial leakage of the optical wave into the GaSb substrate (refractive index ~3.8), resulting in undesirable optical loss and the interference with substrate modes. Hence, if the SL cladding layer can be replaced even partially so with a more appropriate material, the ICL performance will improve significantly in terms of attainable cw output power and reliability.

Alternatively, Al-rich quaternary AlGaAsSb cladding layers were employed in ICLs [48-50] due to its lower refractive index (~3.3 [51]) and somewhat higher thermal conductivity (~7 W/m·K [46]) compared to the SL cladding layer. However, the RT threshold current density J_{th} of ICLs with AlGaAsSb cladding layers was 220 A/cm^2 in the first two initial attempts, which is higher than 134 A/cm^2 that was achieved by a similar ICL with the SL cladding layers [20]. Additionally, ICLs with AlGaAsSb cladding layers had a larger threshold voltage V_{th} with a lower voltage efficiency due probably to the higher bandgap of AlGaAsSb. Recently, the device performance of ICLs with AlGaAsSb cladding layers was substantially improved with a J_{th} of 130 A/cm^2 at 20°C with a cavity length of 2.9 mm [50]. However, the threshold voltage remained relatively high (~4.12 V) for a 5-stage device operating near 3.4 μm, corresponding to a voltage efficiency of 44%, which is much less than state-of-the-art GaSb-based ICLs (~80%) with the traditional SL cladding. The AlGaAsSb cladding layers were commonly used in conventional GaSb-based type-I QW lasers [52-53] and have been used for type-I ICLs with excellent device performance [54-55]. Hence, there should still be potential for AlGaAsSb cladding layers to be explored in type-II ICLs to advance the device performance further.

On the other hand, heavily doped semiconductors, such as n^+-type InAs, can have a much lower refractive index and should be effective optical cladding materials for achieving superior confinement. Heavily doped n^+-type InAs layers were first adopted as cladding layers in plasmon enhanced waveguide QCLs [56-58] but should be more favorable for the transverse electric (TE) polarization of ICLs in contrast to the transverse magnetic (TM) polarization of QCLs. Initial development and study of InAs-based ICLs were carried out from 2008 at the University of Oklahoma [39-40, 59-61]. However, the tradeoff in using the heavily doped InAs comes at the cost of a much larger free-carrier absorption loss. To alleviate such a loss, early InAs-based plasmon waveguide ICLs used relatively thick (*e.g.*, >1 μm) undoped InAs layers as separate confinement layers (SCLs). This resulted in a significant portion of the optical intensity profile residing in the thick SCL region leading to a reduction of the optical confinement within the cascade active region, which lowered the attainable optical gain. Therefore, although lasing was demonstrated in a wide wavelength range beyond 11 μm, desirable device performance such as high output power with low threshold current and especially cw operation at RT, has not been achieved in these plasmon waveguide ICLs. To improve upon this, the InAs/AlSb SL layer was introduced again in 2015 as an intermediate cladding layer to replace a portion of the undoped InAs SCL in the plasmon waveguide ICLs [36], which enhanced the optical confinement with the gain region and suppressed the extent of the optical wave into the plasmon cladding, simultaneously reducing the free-carrier loss in the n^+-InAs outer cladding layers. Consequently, the threshold current density of these ICLs with the so-called hybrid cladding was reduced substantially with cw operation at RT and above [36] and with a high voltage efficiency (>85% [37]) demonstrated. Later, this approach was explored in long wavelength InAs-based ICLs [21, 42-44,62] with improved device performance and GaSb-based ICLs in the wavelength range of 4 to 6 μm [63-64]. A GaSb-based ICL with the hybrid cladding layer showed a RT threshold current density of 220 A/cm^2 at a wavelength near 4.8 μm [63], breaking the previous record of 247A/cm^2 obtained from InAs-based ICLs. For the GaSb-based ICLs with the hybrid cladding layers, heavily *n*-type doped $InAs_{0.91}Sb_{0.09}$ (lattice matched to GaSb) plasmon layers were used instead of heavily n-doped InAs for the outer cladding, while the InAs/AlSb SL was used as the intermediate cladding and had a reduced thickness. The SCL was formed

from relatively lightly n-doped GaSb. The thermal conductivity of InAsSb (15 W/(m·K) [65]) is approximately five times that of a SL cladding layer, which should help to improve the thermal dissipation of the GaSb-based ICLs. Recently, we applied this hybrid cladding layer approach to GaSb-based ICLs in the 3-4 μm wavelength region and obtained encouraging results [66]. However, due mainly to the significant deviations (>10%) in layer thicknesses during MBE growth from the designed values, the device performance did not meet expectations. Hence, to investigate how well GaSb-based ICLs in this wavelength range can perform with the hybrid cladding layers, two new ICL wafers were recently grown and corresponding devices were made from them. As will be described below, the devices showed substantially improved device performance with the hybrid cladding layers, suggesting promising potential of this hybrid cladding approach.

2. Material Growth and Device Fabrication

Two ICL wafers, Y088L and Y089L, were grown by MBE using a Veeco GENxplor with As and Sb supplied from valved cracking sources, in order to achieve good agreement in grown layer thicknesses with the designed values. They are based on the same designs that were used for previous ICL wafer Y086L [66]. All of the ICL wafers reported here have six cascade stages (N_c) with a commonly adopted W-QW [4, 67] active region consisting of a layer sequence of AlSb/InAs/$Ga_{0.6}In_{0.4}Sb$/InAs/AlSb (25/16.5/28/14/12 in Å) in the growth direction. They all shared a similar design except the thicknesses of the GaSb layers in the hole injectors for Y089L were increased by ~10% compared to that for Y086L and Y088L. This difference may affect the carrier transport and other device performance characteristics. The increase of the GaSb QW thicknesses will shift the hole levels toward the valence band edge of GaSb to widen the interband tunneling window [68] under a forward bias voltage,

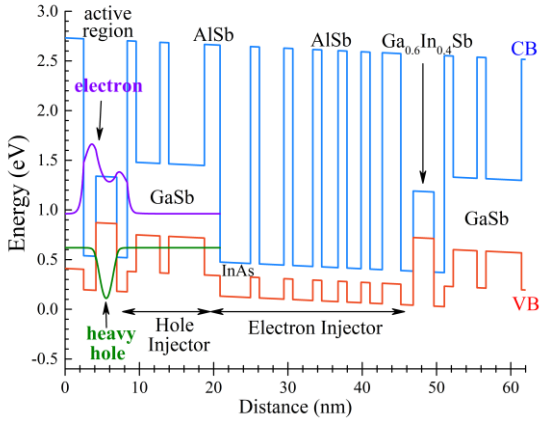

Fig. 2 Band diagram and layer structure of cascade stage. For wafer Y088L, the thickness (in unit of Å) of each layer in one stage beginning at the barrier separating the electron injector and the active region is 25, 16.5, 28, 14, 12, 32, 12, 48, 21, 41, 12, 33, 12, 27, 12, 22, 12, 19, 12 and 16.5.

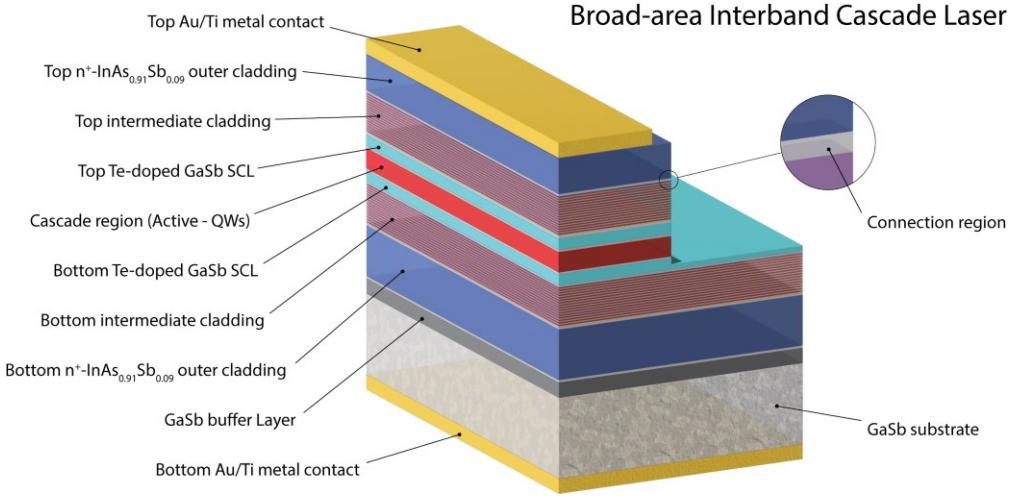

Fig. 3 A schematic layer structure of a broad-area ICL device with hybrid cladding layers, showing various functional segments and metal contacts.

leading to a reduced voltage for smooth transport. The effects of this will be discussed in section 3. The band edge diagram for one and a half cascade periods is shown in Fig. 2 for wafer Y088L, where the center 4 QWs in the electron injector were doped with Si at 4.3×10^{18} cm^{-3} based on the perspective of carrier rebalancing [15]. The cascade stages are sandwiched between two 2100 Å-thick lightly Te doped (2.7×10^{17} cm^{-3}) GaSb SCLs and two 0.75-µm-thick n-doped ($1.5\times10^{17}cm^{-3}$) InAs/AlSb intermediate SL cladding layers, followed by 1.0-µm-thick bottom and 0.75-µm-thick top n^{+}-doped ($3.2\times10^{19}cm^{-3}$) $InAs_{0.91}Sb_{0.09}$ layers as shown in Fig. 3. The InAs/AlSb connection regions between main functional segments are illustrated in the inset.

The material quality of these ICL wafers and the surface morphology were examined by X-ray diffraction (XRD) and differential-interference-contrast microscopy (DIC). The DIC analysis showed a defect density range of 2.4×10^{3} to 3.5×10^{3} cm^{-2} across the two new ICL wafers (Y088L and Y089L). Fig. 4. depicts the measured (blue) x-ray diffraction patten for wafer Y088L and the corresponding simulated pattern (orange), exhibiting close agreement. The measured x-ray diffraction patten for wafer Y089L is similar. According to the satellite peaks, the extracted InAs/AlSb SL period in Y088L and Y089L was thinner by 1.2% and 2.2% than the design, respectively. Furthermore, the cascade region in Y088L was about 1.5% thinner than intended, while the cascade region in Y089L was thinner by just 0.075%. Compared to the significant deviations of the SL and cascade region layer thicknesses observed from the previous ICL wafers [66], the layer thickness errors in the two new wafers were greatly reduced. Table 1 presents a comprehensive comparison of the measured structural deviations and performance features for three of the ICL devices measured at 300 K, including their maximum cw operating temperatures $T_{cw,max}$.

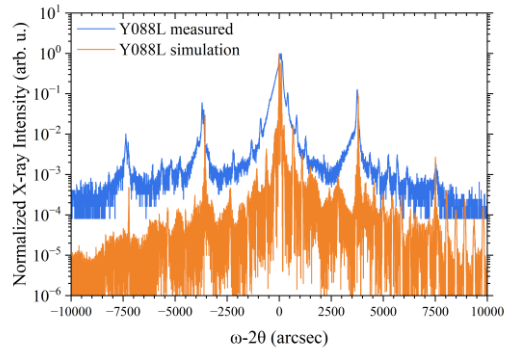

Fig. 4 The experimental measured XRD pattern for Y088L (blue) with corresponding simulation results (orange). The origin for the x-axis is at (004) peak for the GaSb substrate.

Table 1. Summary of layer thickness and the best device performance features at 300 K.

Wafer	Thickness deviation		λ (µm)	J_{th} (A/cm^2)	V_{th} (V)	η_v (%)	$T_{cw,max}$ (K)
	SL (%)	Cascade (%)					
Y086L	+16.2	+13.4	3.824	154	3.02	64.4	260
Y088L	-1.2	-1.5	3.620	134	2.73	74.9	278
Y089L	-2.2	+0.075	3.615	138	2.78	73.4	273

Pieces from the two wafers were fabricated into 100-µm-wide (e.g., Y088LBA1-2B and Y089LBA1-4G) and 150 µm-wide (e.g., Y088LBA1-4C and Y089LBA1-3C) broad area (BA) mesas using wet chemical etching and standard UV contact photolithography. They were then cleaved into laser bars with cavity lengths (L) of approximately 2 mm and 3 mm. The substrates were not thinned nor were the facets coated. The laser bars were mounted epi-side up on copper heat sinks for testing.

3. Device performance results and discussion

Emission spectra from the fabricated ICLs were obtained using a Nicolet 8700 Fourier transform infrared spectrometer (FTIR). A PM3 Coherent PowerMax thermopile power meter was used to collect the cw output power of the ICLs, in which the beam divergence loss was not included. Hence, the reported output power and EQE of the devices presented later are conservative. Fig. 5 summarizes the threshold characteristics of many devices made from both ICL wafers, which were able to operate in cw and pulsed modes. Among them, Y088LBA1-1F, Y088LBA1-4C, Y088LBA1-4D, and Y089LBA1-3C are 150-μm-wide devices, while the other devices are 100-μm-wide devices. In cw operation, there were noticeable variations in the threshold current density (J_{th}) and maximum operating temperature, which we attribute to heating effects within the devices due to various device size as well as possible nonuniformities among the wafers. In pulsed operation with 1 μs pulses at a repetition rate of 5 kHz in the temperature range from 200 to 360 K, the devices exhibited quite similar J_{th} values, which were somewhat lower with the 3-mm cavity length due to a smaller mirror loss compared to the 2-mm cavity. In this temperature range, the characteristic temperature (T_0) is estimated to be about 56 K for the 3-mm-long devices from wafer Y088L, and 54 K for the devices from wafer Y089L. These values are higher than the T_0 of~ 48 K reported in Ref. 66 for devices from the early wafer Y086L. When the devices were operated above 360 K, the heating became non-negligible under pulsed operation due to the large (~ several Amperes) injection current required to achieve lasing along with a relatively high threshold voltage (>5 V), and consequently the J_{th} increased with temperature at a fast pace. Nevertheless, the relatively small (100 μm×2 mm) BA devices Y088LBA1-1H and Y088LBA1-2B could still be operated at temperatures above 380 K or even slightly above 400 K. At 395 K and above, the pulse width was reduced to 200 ns to minimize the heating. Compared to devices made from previous ICL wafers [66], the devices from the two new wafers could operate over a wider temperature range and had reduced threshold current densities in pulsed operation at 300 K and above as shown in Table 1 and Fig. 5. In the following subsections, detailed performance characteristics for the representative devices from each of the new ICL wafers will be described and discussed.

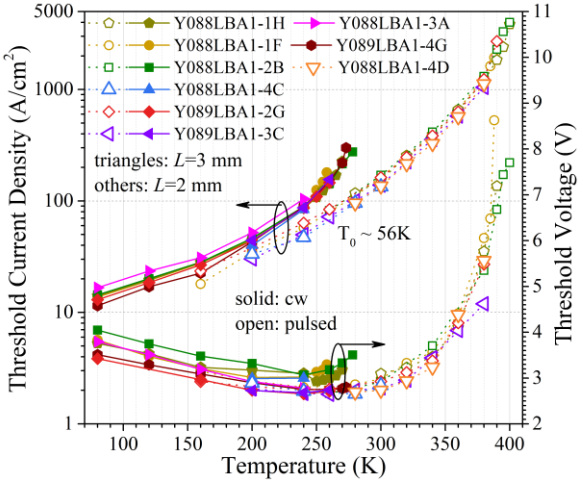

Fig. 5 Threshold current density (J_{th}) and threshold voltage (V_{th}) as a function of temperature for devices from the two new ICL wafers.

3.1. Device performance of Y088L

As shown in Fig. 6, a representative 100-μm-wide and 2-mm-long device (Y088LBA1-2B) lased in cw mode from 80 K with an emission wavelength of 3.18 μm up to 278 K at 3.63 μm with a J_{th} of 275 A/cm^2 and a V_{th} of 3.5 V, corresponding to a voltage efficiency (η_v) of 59%. This $T_{cw,max}$ of 278 K is 18 K higher than the maximum cw operating temperature of 260 K for ICLs made from the early wafer Y086L [66], and is the highest cw operating temperature ever

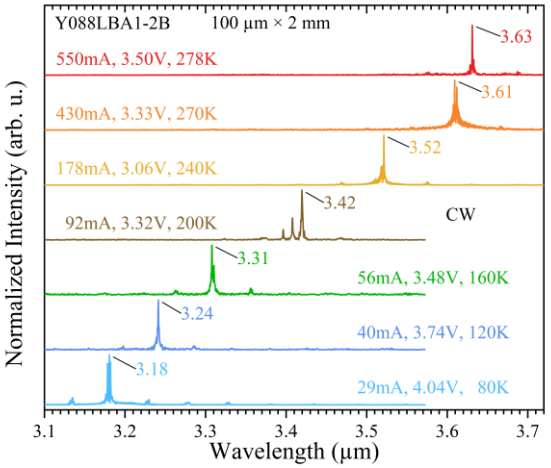

Fig. 6 The cw lasing spectra for Y088LBA1-2B along with the threshold current and threshold voltage and emission wavelength at each temperature.

reported among BA epi-side up mounted type-II ICLs, suggesting improved thermal dissipation due to the hybrid cladding layer approach. This device had a cw threshold current density J_{th} of 14.4 A/cm^2 and a threshold voltage V_{th} of 4.04 V at 80 K, which is acceptable, but significantly higher than the lowest value (2-3 A/cm^2 [21]) reported among BA ICLs at 80 K. Another 150 µm-wide and 3-mm-long device (Y088LBA1-4D) had a smaller J_{th} of 11.5 A/cm^2 due to a smaller mirror loss, which is substantially larger than the J_{th} (~7 A/cm^2) of a 3-mm-long device from the early wafer Y086L. All of these devices have a similar defect density in the range from 1-5×10^3 cm^{-2} from DIC microscopy and are expected to have comparably low Shockley-Read-Hall (SRH) recombination losses, except for a 100 µm-wide and 3-mm-long device Y088LBA1-3A that was cleaved from the edge of the wafer and had a J_{th} of 16.6 A/cm^2 at 80 K. The higher J_{th} for Y088L at 80 K might be related to possible variations in device processing/mounting. Nevertheless, the observed external quantum efficiency (EQE) at all temperatures for devices from Y088L is somewhat higher than that for the device from the early wafer Y086L. For example, the cw current-voltage-light (IVL) characteristics shown in Fig. 7 for device Y088LBA1-1F, yield an extracted EQE of 248% at 80 K, that falls to 101% at 250 K, which is higher than the reported EQE of 210% and 85% for a device from the early wafer Y086L at the same temperatures. This implies the internal optical loss in wafer Y088L could be lower compared to that in Y086L, which may have played an important role in the improved high temperature operation of devices made from Y088L. This will be elaborated below.

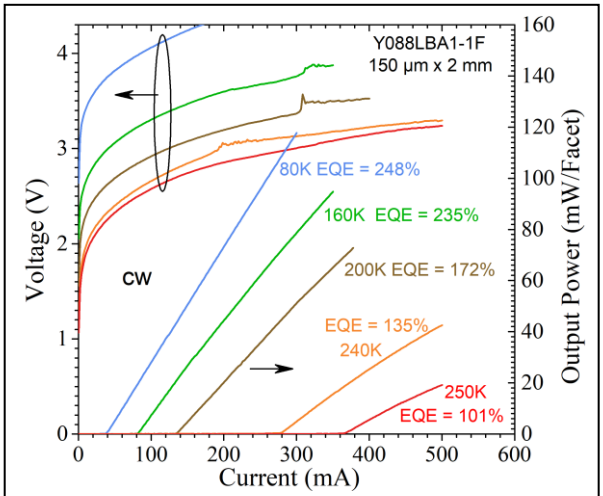

Fig. 7 The cw IVL characteristics for Y088LBA1-1F from 80K to 250K along with the corresponding EQE values.

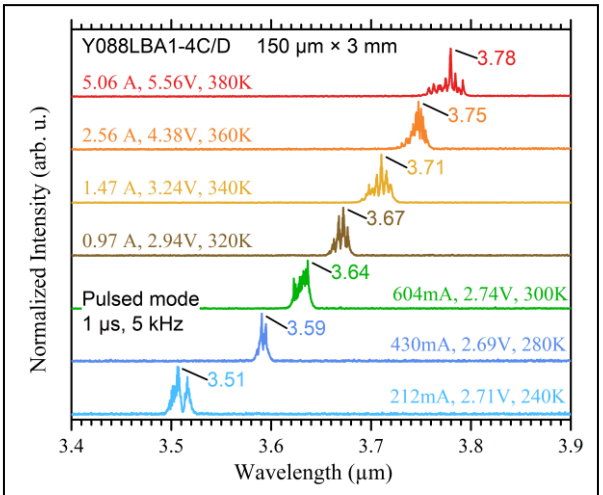

Fig. 8 The pulsed lasing spectra for Y088LBA1-4C/D along with the threshold current, threshold voltage, and emission wavelength at each temperature step.

As mentioned earlier, wafers Y088L and Y086L shared the same design, but the actual SL and cascade layer thicknesses from MBE growth, according to XRD measurements, were more than 10% thicker in the early wafer Y086L, compared to the intended design as shown in Table 1. As XRD can only probe the average cascade period, it can be hard to know exactly where deviations occurred during growth. However, as the strain balance is maintained in the entire structure with an average defect density below 5×10^3 cm^{-2}, it is reasonable to assume a uniform distribution in the growth error of the cascade period. As a result of this increased thickness, the hole levels in the hole injector shifted toward to the GaSb valence band edge and the electron levels in the electron injector shifted towards the InAs conduction band edge, which widened the interband tunneling window between the GaSb valence band edge in the hole injector and the InAs conduction band edge in the electron injector [68] under a given bias voltage, resulting in a smoother carrier transport and a reduced threshold voltage at 80 K. This might be a factor as to why the V_{th} was higher in devices from Y088L at 80 K, as such large structural deviations were remedied in the growth process for the newer ICL wafer. The resulting thinner QW layers in Y088L would require a larger voltage to open up the interband tunneling window, leading to a relatively higher threshold current density at 80 K.

On the other hand, the thicker GaSb layers in the early wafer Y086L provided more space for holes, which may have caused additional absorption loss. This extra absorption loss due to more holes in the GaSb layers could become more significant with increasing temperature, while the interband tunneling window widened with improved carrier transport due to the narrowing of the bandgap at the higher temperatures. Consequently, the threshold current density J_{th} for devices made from Y086L increased with temperature at a faster pace with a lower T_0 (48 K), while the threshold voltage V_{th} for devices made from Y088L decreased in the range from 80 to ~260 K as shown in Fig. 5 and its J_{th} increased with temperature at a slower pace with a higher T_0 (56 K), resulting in relatively low J_{th} at high temperatures as also shown in Fig. 5. For example, device Y088LBA1-4D at 360 K had a pulsed J_{th} of 569 A/cm^2, which is significantly lower than the value (J_{th} = 1100 A/cm^2) for a device from Y086L at the same temperature.

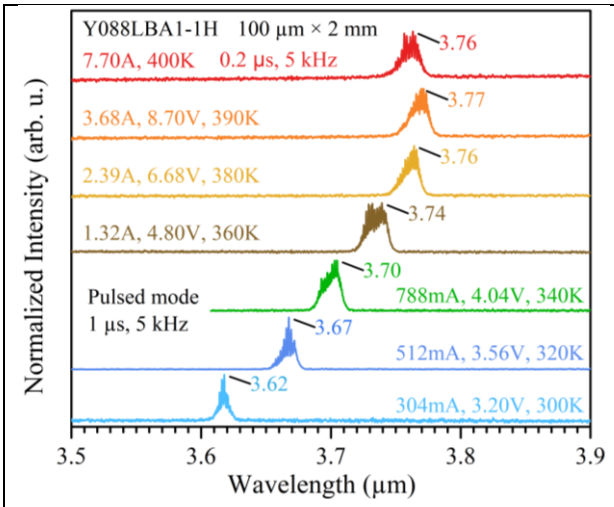

Fig. 9 The pulsed lasing spectra for Y088LBA1-1H along with the threshold current, threshold voltage, and emission wavelength at each temperature step.

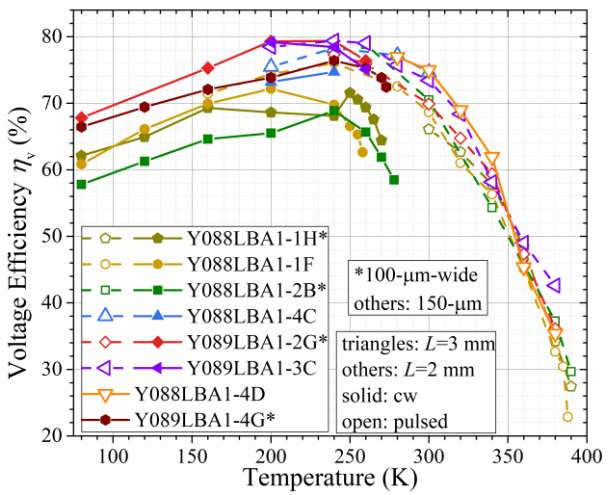

Fig. 10 Voltage efficiency at cw and pulsed modes as a function of temperature for Y088L and Y089L.

In pulsed operation, two 150-μm wide and 3-mm-long devices (Y088LBA1-4C/D as shown in Fig. 8) lased at temperatures up to 380 K, while two 100-μm wide and 2-mm-long devices (Y088LBA1-1H/2B as shown in Fig. 9 and Fig. 5) lased up to 400 K. These devices exhibited an emission wavelength of approximately 3.78 and 3.76 μm at their maximum operating temperatures, with J_{th} = 1120 A/cm^2 and 3850 A/cm^2, respectively. This operating temperature is 20 K higher than that of the device from Y086L. At 300 K, these devices emitted at wavelengths of 3.64 (Fig. 8) and 3.62 μm (Fig. 9) with measured J_{th} of 134 A/cm^2, 152 A/cm^2 (Fig. 9) and 148 A/cm^2 (for Y088LBA1-2B in Fig. 5), respectively. The J_{th} for the comparable 3-mm-long device is 12.9% smaller than that of the device from Y086L, which could be due to the lower absorption loss from the GaSb layers as discussed above. Their V_{th} at 300 K were 2.74 V (Fig. 8) and 2.92 V (for Y088LBA1-2B in Fig. 5), respectively, which for the comparable device is 9.2% lower than that of Y086L. The voltage efficiency η_v for Y088L reached ~75% at 300 K as shown in Fig. 10 and might peak at about 80% near 250 K. The value of η_v is generally higher for the 3-mm-long devices due to their lower J_{th} compared to the 2-mm-long devices. However, for all of them, the voltage efficiencies have a similar non-monotonic relation with temperature. This was due to the improvement of carrier transport with narrowing the bandgap and widening the interband tunneling window when temperature was increased, which resulted in a reduced threshold voltage before J_{th} was increased overwhelmingly. The increase of the voltage efficiency when the temperature was raised from 80 to 240-250 K (depending on individual devices with different sizes) indicates an additional benefit of improved carrier transport with increasing temperature. This behavior was also observed in InAs-based ICLs [37] and should provide helpful guidance in the optimization of ICL performance at the targeted temperature range.

3.2. Device performance of Y089L

A 100-µm-wide and 2-mm-long representative device from the second ICL wafer (Y089LBA1-4G), which included the thicker GaSb hole injector, lased at 80 K in cw mode with an emission wavelength of 3.19 µm, J_{th} of 11.5 A/cm^2, and V_{th} of 3.51 V, as shown in Fig. 11. This V_{th} is 13% lower than that of Y088L, corresponding to a voltage efficiency of 68%, which was higher than achieved (~ 62% at 80 K as shown in Fig. 10) for the device from Y088L. This is attributed to the improved carrier transport from the thicker GaSb layers in the hole injector compared to Y088L, supporting the earlier discussion in subsection 3.1 in comparison with devices from Y086L. This device lased in cw mode at a temperature up to 273 K at an emission wavelength of 3.67 µm with a J_{th} of 300 A/cm^2 and V_{th} of 2.80 V. This temperature is similarly higher than what was previously reported for BA ICLs and again demonstrated the associated improved thermal dissipation with the hybrid cladding layer approach. As shown by the IVL characteristics in Fig. 12 for another representative 100-µm-wide device (Y089LBA1-2G), the extracted EQEs of 231% at 80 K and 126% at 240 K were comparable to, but slightly lower than that for devices from Y088L. This could be due to the extra absorption loss in the thicker GaSb layers discussed above, which resulted in a slightly higher threshold current density at 300 K as shown in Table 1 and a lower T_0 (54 K) in pulsed operation.

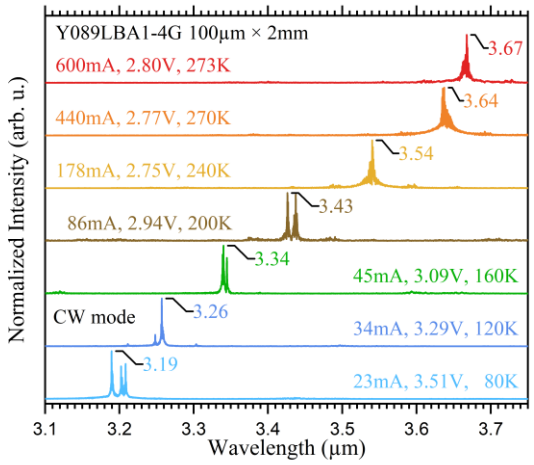

Fig. 11 The CW emission spectra for Y089LBA1-4G along with the threshold current, threshold voltage, and emission wavelength at each temperature.

In pulsed operation with 1 µs pulses at 5 kHz, a 150-µm-wide device (Y089LBA1-3C) lased up to 380 K, while the 100-µm wide devices lased up to 390 K as limited by the pulsed current source. The pulsed spectra for the representative 150-µm-wide and 3-mm-long device Y089LBA1-3C are shown in Fig. 13. At the maximum operating temperature, the 150- and 100-µm wide devices had an emission wavelength of 3.76 µm and 3.77 µm with threshold current densities of J_{th} = 1044 and 2705 A/cm^2, respectively. At 300

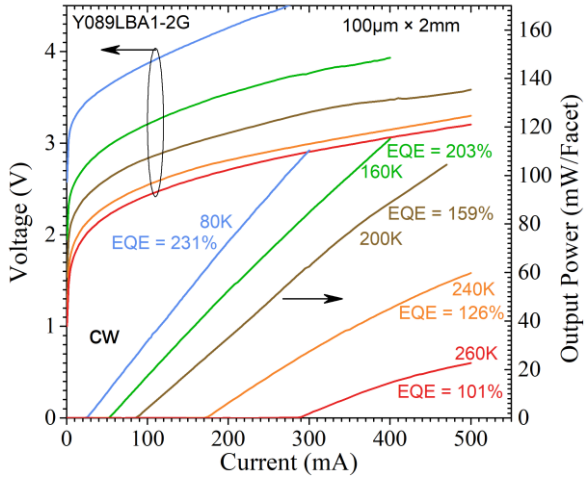

Fig. 12 The cw ICL characteristics for Y089LBA1-2G from 80K to 260K along with the corresponding EQE values.

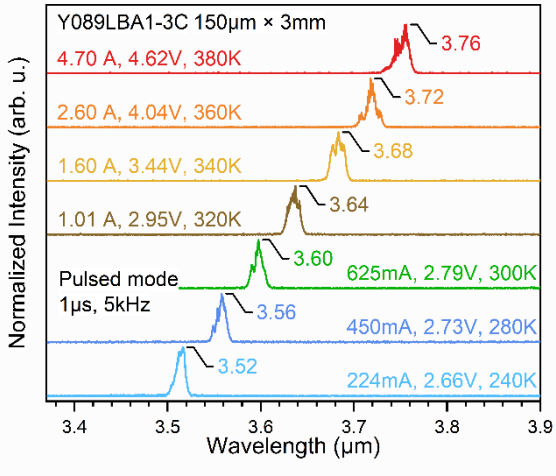

Fig. 13 The pulsed lasing spectra for Y089LBA1-3C along with the threshold current, threshold voltage and emission wavelength at each temperature step.

K, their emission wavelengths were 3.60 μm with J_{th} of 138 A/cm^2 for a 3-mm cavity length and 162 A/cm^2 for a 2-mm cavity length, which are slightly larger values than the J_{th} of Y088L. Their threshold voltages were V_{th} = 2.79 and 2.93 V, respectively, leading to voltage efficiencies of 74% and 70%. Their voltage efficiencies, in most cases as shown in Fig. 10, are slightly larger than their counterparts from the Y088L wafer with thinner GaSb layers in the hole injector, further supporting the improvement of the carrier transport associated with widening the interband tunneling window via increased GaSb layer thickness in the hole injector. Their voltage efficiencies have a similar non-monotonic relation with temperature as shown in Fig. 10, which will be explored by further studies of device performance optimization at a targeted temperature range.

3.3. Modeling and Further Discussion

To evaluate the free-carrier absorption loss and other associated optical properties for these new ICLs, a waveguide simulation was generated based on ICL wafer Y088L at 300 K, as shown in Fig. 14. The small adjustments to the GaSb hole injector layer thickness in the cascade active region for devices from Y089L are not anticipated to affect the overall optical wave profile and the subsequent optical properties of the device. In the simulation, the estimated waveguide loss reported is due only to free-carrier loss, and therefore possible absorption loss due to inter-valence-subband transitions is not included. Also, the effect of a potentially reduced electron concentration due to diffusion of electrons across the injector to recombine with holes is not considered. The displayed results include calculated values of the free-carrier loss (α_i), optical confinement factor (Γ), and the effective refractive index of the waveguide (n_{eff}). The estimated value of the free-carrier absorption loss is 6.67 cm^{-1}, which is slightly higher than the calculated free-carrier absorption loss of 6.52 cm^{-1} for Y086L [66]. It should be noted that devices made from Y086L lased at a longer wavelength of 3.824 μm at 300 K, which might cause more free-carrier absorption loss in the plasmon cladding layers as the emission wavelength was closer to the plasmon wavelength λ_p, despite the three ICL wafers (Y086L, Y088L, and Y089L) having the same electron concentration. However, as indicated in Table 1, the SL cladding layers in Y086L are more than 15% thicker than the designed value, which suppresses the wave penetration into the heavily doped InAsSb layer and consequently can reduce the free-carrier loss from the InAsSb outer cladding layers. Hence, considering the nearly identical free-carrier absorption loss for wafers Y086L and Y088L, the differences in threshold current density at high temperatures might be caused mainly by the possible additional loss from the GaSb layers in the hole injector, which again supports the analyses presented earlier. Besides, due to the substantially increased SL cladding layer, thermal dissipation in Y086L might be worse, which could have contributed to the lower maximum cw operating compared to Y088L. Moreover, this waveguide structure was initially designed for devices emitting at 3.3 μm at 300 K, but devices made from the two new wafers lased at 3.6 μm, which is 0.3 μm longer than the targeted value. Since this waveguide is not optimally designed for this emission wavelength, the optical field leaks more into the high-doped plasmon cladding layer with a 30% higher free-carrier absorption loss than the intended design of ~5.13 cm^{-1}. Hence, the device performance of ICLs with the hybrid cladding layer can be improved further with adjustments of the waveguide parameters.

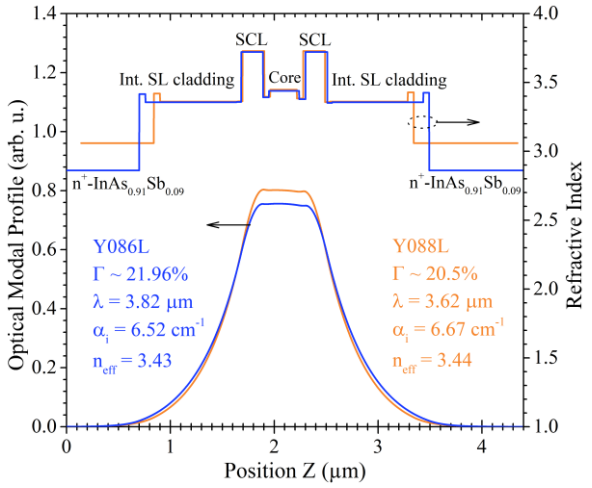

Fig. 14 The calculated optical modal profile and refractive index for Y088L at 300K and the observed lasing wavelength.

4. Summary and Concluding Remarks

By briefly reviewing the development of ICLs, long-standing issues related to the SL cladding layer were discussed with possible solutions and efforts. Focusing on the hybrid cladding layer approach, devices made from two recently grown ICL wafers were investigated and compared with previously reported ICLs. Significantly improved device performance was achieved for these ICLs with hybrid cladding layers. This includes cw operation of a BA device up to 278 K, the highest among reported BA type-II ICLs, suggesting improved thermal dissipation with the hybrid cladding approach. Also, despite the possible high free-carrier absorption loss from the heavily doped n^+-$InAs_{0.91}Sb_{0.09}$ outer cladding layer and a non-optimal waveguide, the threshold current density was as low as 134 A/cm^2 at 300 K, similar to that from state-of-the-ICLs with traditional SL cladding layers. Furthermore, these ICLs exhibited a substantially reduced threshold voltage with a peak voltage efficiency of 80%, which is more than a 10% increase compared to similar ICLs reported earlier [66]. On the other hand, through comparative study of ICLs with different layer thicknesses of GaSb QWs in the hole injector, an interesting relation between the carrier transport, threshold voltage and additional hole-induced absorption loss was revealed and discussed. Its temperature dependence, as reflected by a non-monotonic relationship between the voltage efficiency and temperature, may shed light that can guide device optimization for operation at a targeted temperature range. These findings and improved device performance features suggest significant room for ICLs with the hybrid cladding to advance further. Additionally, this ICL configuration with the highly doped InAsSb outer cladding layer will be beneficial to lateral current conduction when the ICL structure is grown on a semi-insulating substrate such as Si [69] or GaAs.

Acknowledgement

This work was partially supported by NSF (No. ECCS-1931193) and The Oklahoma Center for the Advancement of Science and Technology (OCAST) Award AR21-024.

References

1. R. Q. Yang, “Infrared laser based on intersubband transitions in quantum wells,” poster P3.80 at *7th Inter. Conf. on Superlattices, Microstructures and Microdevices*, Banff, Canada, August 22-26, 1994.
2. R. Q. Yang, “Infrared laser based on intersubband transitions in quantum wells,” Superlattices and Microstructures, **17**, 77-83 (1995).
3. G. A. Sai-Halasz, R. Tsu, and L. Esaki, “A new semiconductor superlattice”, Appl. Phys. Lett. **30**, 651 (1977).
4. L. Esaki, L. L. Chang, and E. E. Mendez, “Polytype superlattices and multi-heterojunctions”, Jpn. J. Appl. Phys., **20**, L529 (1981).
5. J. Faist, F. Capasso, D. L. Sivco, C. Sirtori, A. L. Hutchinson, and A. Y. Cho, “Quantum cascade laser”, *Science* **264**, 553 (1994).
6. J. R. Meyer, I. Vurgaftman, R. Q. Yang, and L. R. Ram-Mohan, “Type-II and type-I interband cascade lasers”, Electronics Letters, **32**, 45-46 (1996).
7. R. Q. Yang, and S. S. Pei, "Novel type-II quantum cascade lasers", J. Appl. Phys. **79**, 8197 (1996).
8. C.-H. Lin, R. Q. Yang, D. Zhang, S. J. Murry, S. S. Pei, A. A. Allerman, and S. R. Kurtz, “Type-II interband quantum cascade laser at 3.8 μm,” Electron. Lett. **33**, 598 (1997).
9. R. Q. Yang, “Novel Concepts and Structures for Infrared Lasers”, Chap. 2, in *Long Wavelength Infrared Emitters Based on Quantum Wells and Superlattices*, edited by M. Helm (Gordon & Breach Pub., Singapore, 2000), and references therein.
10. R. Q. Yang, “Mid-Infrared Interband Cascade Lasers Based on Type-II Heterostructures”, Microelectronics J. **30**, 1043 (1999).
11. R. Q. Yang, J. L. Bradshaw, J. D. Bruno, J. T. Pham, D.E. Wortman, “Mid-IR type-II interband cascade lasers”, IEEE J. Quantum Electron. **38**, 559 (2002).

12. K. Mansour, Y. Qiu, C. J. Hill, A. Soibel, R. Q. Yang, "Mid-IR interband cascade lasers at thermoelectric cooler temperatures", Electronics Letters, **42** (18), 1034 (2006).
13. M. Kim, C. L. Canedy, W. W. Bewley, C. S. Kim, J. R. Linda, J. Abell, I. Vurgaftman, and J. R. Meyer, "Interband cascade laser emitting at λ=3.75 μm in continuous wave above room temperature", Appl. Phys. Lett. **92**, 191110 (2008).
14. A. Bauer, M. Dallner, M. Kamp, S. Hofling, L. Worschech, and A. Forchel, "Shortened injector interband cascade lasers for 3.3- to 3.6-μm emission", Optical Engineering, **49**, 111117 (2010).
15. I. Vurgaftman, W. W. Bewley, C. L. Canedy, C. S. Kim, M. Kim, C. D. Merritt, J. Abell, J. R. Lindle, and J. R. Meyer, "Rebalancing of internally generated carriers for mid-infrared interband cascade lasers with very low power consumption", Nature Communications, **2**, 585 (2011).
16. Rui Q. Yang, "Interband Cascade (IC) Lasers", Chap. 12, in *Semiconductor lasers: fundamentals and applications*, edited by A. Baranov and E. Tournie (Woodhead Publishing Limited, Cambridge, UK, 2013).
17. I. Vurgaftman, W. W. Bewley, C. L. Canedy, C. S. Kim, M. Kim, C. D. Merritt, J. Abell, and J. R. Meyer, "Interband cascade lasers with low threshold powers and high output powers", *IEEE J. Select. Top. Quantum Elctron.,* **19**(4): 1200210. (2013).
18. R. Weih, M. Kamp, and S. Hofling, "Interband cascade lasers with room temperature threshold current densities below 100 A/cm^2", *Appl. Phys. Lett.,* **102**(23): 231123 (2013).
19. C. L. Canedy, J. Abell, C. D. Merritt, W. W. Bewley, C. S. Kim, M. Kim, I. Vurgaftman, and J. R. Meyer, "Pulsed and CW performance of 7-stage interband cascade lasers", *Opt.Express,* **22**(7): 7702 (2014).
20. I. Vurgaftman, R. Weih, M. Kamp, J R Meyer, C. L. Canedy, C. S. Kim, M. Kim, W. W. Bewley, C. D. Merritt, J. Abell and S. Höfling, "Interband cascade lasers", J. Phys. D: Appl. Phys. **48** 123001 (2015).
21. R. Q. Yang, L. Li, W. Huang, S.M.S. Rassel, J. A. Gupta, A. Bezinger, X. Wu, S.G. Razavipour**,** G. C. Aers, "InAs-based Interband Cascade Lasers", IEEE J. Selected Topics Quantum Electronics, **25**, No. 6, 1200108 (2019).
22. J. R. Meyer, W. W. Bewley, C. L. Canedy, C. S. Kim, M. Kim, C. D. Merritt, and I. Vurgaftman, "The interband cascade laser", Photonics. **7**, 75 (2020).
23. H. Knotig, J. Nauschutz, N. Opacak, S. Hofling, J. Koeth, R. Weih, and B. Schwarz, "Mitigating valence intersubband absorption in interband cascade lasers", Laser & Photonics Reviews, 2200156 (2022).
24. J. Nauschütz, H. Knotig, R. Weih, J. Scheuermann, J. Koeth, S. Hofling, and B. Schwarz, "Pushing the Room Temperature Continuous-Wave Operation Limit of GaSb-Based Interband Cascade Lasers beyond 6 μm," Laser Photonics Rev **17**(4), 2200587 (2023).
25. R. Q. Yang, C. J. Hill, K. Mansour, Y. Qiu, A. Soibel, R. Muller and P. Echternach, "Distributed feedback mid-infrared interband cascade lasers at thermoelectric cooler temperatures", IEEE J. Selected Topics of Quantum Electronics, **13**, 1074 (2007).
26. I. Vurgaftman, W. W. Bewley, C. D. Merritt, C. L. Canedy, M. V. Warren, C. S. Kim and J. R. Meyer, "Sensitive Chemical Detection with Distributed Feedback Interband Cascade Lasers", Encyclopedia of Analytical Chemistry (2016).
27. J. Koeth, R. Weih, J. Scheuermanna, M. Fischera, A. Schadeb, M. Kamp, S. Höfling, "Mid infrared DFB interband cascade lasers", Proc. SPIE, **10403**, 1040308 (2017).
28. M. Horstjann, Y. A. Bakhirkin, A. A. Kosterev, R. F. Curl, F. K. Tittel, C. M. Wong, C. J. Hill, and R. Q. Yang, "Formaldehyde Sensor using Interband Cascade Laser based Quartz-enhanced Photoacoustic Spectroscopy", Appl. Phys. B **79**, 799 (2004).
29. G. Wysocki, Y. Bakhirkin, S. So, F. K. Tittel, C. J. Hill, R. Q. Yang, and M. P. Fraser "Dual Interband Cascade Laser based trace gas sensor for environmental monitoring", Appl. Optics. **46**, 8202 (2007).
30. L. E. Christensen, C. R. Webster, R. Q. Yang, "Aircraft and Balloon *in Situ* Measurements of Methane and Hydrochloric Acid Using Interband Cascade Lasers", Applied Optics **46**, 1132 (2007).

31. L. E. Christensen, K. Mansour, and R. Q. Yang, "Thermoelectrically cooled interband cascade laser for field measurements", Optical Engineering, **49**, 111119 (2010).
32. K. R. Parameswaran, D. I. Rosen, M. G. Allen, A. M. Ganz, T. H. Risby, "Off-axis integrated cavity output spectroscopy with a mid-infrared interband cascade laser for real-time breath-ethane measurements," Appl. Opt. **48**(4), B73-B79 (2009).
33. C. R. Webster, P. R. Mahaffy, S. K. Atreya, G. J. Flesch, M. A. Mischna, P.-Y. Meslin, K. A. Farley, P. G. Conrad, L. E. Christensen, A. A. Pavlov, the MSL Science Team, "Mars methane detection and variability at Gale crater", Science **347**, 415 (2015).
34. R. Ghorbani and F. M. Schmidt, "ICL-based TDLAS sensor for real-time breath gas analysis of carbon monoxide isotopes", Optical Express, **25**, 12743 (2017).
35. K. Tanaka, K. Akishima, M. Sekita, K. Tonokura, M. Konno, "Measurement of ethylene in combustion exhaust using a 3.3-μm distributed feedback interband cascade laser with wavelength modulation spectroscopy", Appl. Phys. B **123**, 219 (2017).
36. L. Li, Y. Jiang, H. Ye, R. Q. Yang, T. D. Mishima, M.B. Santos, and M. B. Johnson, "Low-threshold InAs-based interband cascade lasers operating at high temperatures," Appl. Phys. Lett, **106**, 251102 (2015).
37. K. Zhang, Y. Lin, W. Zheng, R. Q. Yang, H. Lu, Y. F. Chen, "Low threshold InAs-based interband cascade lasers grown by MBE", J. Crystal Growth, **586**, 1266185 (2022).
38. W. Huang, S. Hu, J. Tu, *et al*., "High-temperature continuous-wave operation of InAs-based interband cascade laser", Appl. Phys. Lett, **123**, 151111 (2023).
39. Z. Tian, R. Q. Yang, T. D. Mishima, M. B. Santos, M. B. Johnson, "Plasmon-waveguide interband cascade lasers near 7.5 μm" IEEE Photo. Technol. Lett. **21**, 1588 (2009).
40. L. Li, H. Ye, Y. Jiang, R. Q. Yang, J. C. Keay, T. D. Mishima, M.B. Santos, and M. B. Johnson, "MBE Growth MBE Grown Long-wavelength Interband Cascade Lasers on InAs Substrates," J. Crystal Growth, **425**, 369-372 (2015).
41. M. Dallner, F. Hau, S. Höfling, M. Kamp, "InAs-based interband-cascade-lasers emitting around 7 μm with threshold current densities below 1 kA/cm^2 at room temperature", Appl. Phys. Lett., **106**, 041108 (2015).
42. J. A. Massengale, Y. Shen, R. Q. Yang, S. D. Hawkins, and J. F. Klem, "Long wavelength interband cascade lasers," Appl. Phys. Lett. **120**, 091105 (2022).
43. J. A. Massengale, Y. Shen, R. Q. Yang, S. D. Hawkins, and J. F. Klem, "Enhanced Performance of InAs-based Interband Cascade Lasers Emitting between 10-13 μm," Semiconductor Science and Technology **38**, 025009 (2023).
44. Y. Shen, J. A. Massengale, R. Q. Yang, S. D. Hawkins, and A. J. Muhowski, "Pushing the Performance Limits of Long Wavelength Interband Cascade Lasers using Innovative Quantum Well Active Regions", Appl. Phys. Lett. **123**, 041108 (2023).
45. T. Borca-Tasciuc, D. Achimov, W. L. Liu, G. Chen, H.-W. Ren, C.-H. Lin, and S. S. Pei, "Thermal conductivity of InAs/AlSb superlattices", Microscale Thermophys. Eng. **5**, 225 (2001).
46. D. W. Song, J. R. Meyer, I. Vurgaftman, M.-J. Yang, B. Z. Nosho,L. J. Whitman, H. Lee, R. U. Martinelli, G. W. Turner, M. J. Manfra and G. Chen "Thermal conductivity of $AlAs_{0.07}Sb_{0.93}$ and $Al_{0.9}Ga_{0.1}As_{0.07}Sb_{0.93}$ alloys and $(AlAs)_1/(AlSb)_{11}$ digital-alloy superlattices", J. Appl. Phys. **92**, 4994 (2002).
47. C. Zhou, B. Cui, C. L. Canedy, C. S. Kim, M. Kim, W. W. Bewley, C. D. Merritt, J. Abell, J. R. Meyer, and M. Grayson, "Thermal conductivity tensors of the cladding and active layers of interband cascade lasers," Appl. Phys. Lett. **105** (26), 261905 (2014).
48. R. Weih, A. Bauer, M. Kamp, and S. Höfling, "Interband cascade lasers with AlGaAsSb bulk cladding layers," *Opt. Mater. Exp.*, vol. 3, 1624, Oct. 2013, doi: 10.1364/ome.3.001624.
49. D. A. Díaz-Thomas *et al.*, "Interband cascade Lasers with AlGaAsSb cladding layers emitting at 3.3 microm," *Opt Exp.*, vol. 27, 31425–31434, Oct. 2019, doi: 10.1364/OE.27.031425.

50. X. Zhao et al., "High Performance Interband Cascade Lasers with AlGaAsSb Cladding Layers," in IEEE Photonics Technology Letters, vol. 34, no. 5, 291-294, 1 March, 2022, doi: 10.1109/LPT.2022.3153334.
51. S. Adachi, "Band gaps and refractive indices of AlGaAsSb, GaInAsSb, and InPAsSb: Key properties for a variety of the 2–4 μm optoelectronic device applications," J. Appl. Phys. **61**(10), 4869 (1987).
52. G. Belenky, L. Shterengas, M.V. Kisin, and T, Hosoda, "Gallium antimonide (GaSb)-based type-I quantum well diode lasers: recent development and prospects", Chap. 11, in *Semiconductor Lasers: Fundamentals and Applications*, edited by A. Baranov and E. Tournie (Woodhead Publishing Limited, Cambridge, UK, 2013).
53. K. Vizbaras, A. Vizbaras, A. Andrejew, C. Grasse, S. Sprengel and M.-C. Amann, "Room-temperature type-I GaSb-based lasers in the 3.0 – 3.7 μm wavelength range", Proc. SPIE **8277**, 82771B (2012); and references therein.
54. L. Shterengas, R. Liang, G. Kipshidze, T. Hosoda, S. Suchalkin, and G. Belenky, "Type-I quantum well cascade diode lasers emitting near 3 μm", Appl. Phys. Lett. **103**, 121108 (2013).
55. L. Shterengas, G. Kipshidze, T. Hosoda, R. Liang, T. Feng, M. Wang, A. Stein, and G. Belenky, "Cascade Pumping of 1.9-3.3 μm Type-I Quantum Well GaSb-based Diode Lasers", IEEE Journal of Selected Topics in Quantum Electronics, **23** (6), 1500708 (2017); and references therein.
56. K. Ohtani, and H. Ohno, "An InAs-Based Intersubband Quantum Cascade Laser", *Jpn. J. Appl. Phys*. **41**, L1279 (2002).
57. R. Teissier, D. Barate, A. Vicet, C. Alibert, A. N. Baranov, X. Marcadet, C. Renard, M. Garcia, C. Sirtori, D. Revin, and J. Cockburn, "Room temperature operation of InAs/AlSb quantum cascade lasers", *Appl. Phys. Lett*. **85**, 167 (2004).
58. A. N. Baranov and R. Teissier, "Quantum cascade lasers in the InAs/AlSb material system," IEEE J. Sel. Top. Quantum Electron. **21**(6), 1200612 (2015).
59. Z. Tian, R. Q. Yang, T. D. Mishima, M. B. Santos, R. T. Hinkey, M. E. Curtis, and M. B. Johnson, "InAs-based interband cascade lasers near 6 μm", Electron. Lett. **45**, 48 (2009).
60. R. T. Hinkey, Z. Tian, R. Q. Yang, T. D. Mishima, and M. B. Santos, "Reflectance spectrum of plasmon waveguide interband cascade lasers and observation of the Berreman effect", J. Appl. Phys. **110**, No. 4, 043113 (2011).
61. R. Q. Yang, L. Li, L. Zhao, Y. Jiang, Z. Tian, H. Ye, R. T. Hinkey, C. Niu, T. D. Mishima, M. B. Santos, J. C. Keay, M. B. Johnson, K. Mansour, "Recent progress in development of InAs-based Interband Cascade Lasers" Proc. SPIE **8640**, paper 86400Q (2013).
62. J. A. Massengale, Y. Shen, R. Q. Yang, S. D. Hawkins, and A. J. Muhowski, "Low threshold, long wavelength interband cascade lasers with high voltage efficiencies," IEEE J. Quantum Electron., **59**, 2000507 (2023).
63. C. L. Canedy, M. V. Warren, C. D. Merritt, W. W. Bewley, C. S. Kim, M. Kim, I. Vurgaftman, and J. R. Meyer, "Interband cascade lasers with longer wavelengths", Proc. SPIE, **10111**, 101110G (2017).
64. Y. Lin, J. A. Massengale, W. Huang, R. Q. Yang, T. D. Mishima, and M. B. Santos, "Examination of the durability of interband cascade lasers against structural variations," J. Infrared Millimeter Waves **39**, 137 (2020).
65. C. Zhou, I. Vurgaftman, C. L. Canedy, C. S. Kim, M. Kim, W. W. Bewley, C. D. Merritt, J. Abell, J. R. Meyer, A. Hoang, A. Haddadi, M. Razeghi, and M. Grayson, "Thermal conductivity tensors of the cladding and active layers of antimonide infrared lasers and detectors", Optical Materials Express **3**, 1632 (2013).
66. J. A. Massengale, Y. Shen, R. Q. Yang, T. D. Mishima, and M. B. Santos, "Interband cascade lasers with advanced waveguides operating in the 3-4 μm wavelength region," Optical Engineering, **62**, 086103 (2023).
67. J.R. Meyer, C.A. Hoffman, F.J. Bartoli, L.R. Ram-Mohan, "Type-II quantum-well lasers for the mid-wavelength infrared", Appl. Phys. Lett., **67**, 757 (1995).

68. R. Q. Yang, “Electronic States and Interband Tunneling Conditions in Type-II Quantum Well Heterostructures”, J. Appl. Phys. **127**, 025705 (2020).
69. L. Cerutti, D. A. D. Thomas, J. Rodriguez, M. R. Calvo, G. Patriarche, A. N. Baranov, and E. Tournié, "Quantum well interband semiconductor lasers highly tolerant to dislocations," Optica **8**, 1397-1402 (2021).